Corrosion of Old Overhead Lines: Insights into Aluminum-Steel Galvanic Couple Using Electrochemical Techniques

Divino Salvador Ramírez Rico, Stéphane Heurtault, Julien Said, Yuelin Xie, Mireille Turmine, Vincent Vivier

Corrosion of Old Overhead Lines: Insights into Aluminum-Steel Galvanic Couple Using Electrochemical Techniques

Divino Salvador Ramírez Rico,[1] Stéphane Heurtault,[2] Julien Said,[2] Yuelin Xie,[1] Mireille Turmine,[1] Vincent Vivier[1]

[1.] Sorbonne Université, CNRS, Laboratoire de Réactivité de Surface, Paris, France

[2.] Réseau de Transport et d'Électricité, CNER – Département Liaisons, Immeuble Window, 7C Place du Dôme, Paris la Défense cedex, 92073, France

Abstract

In order to explain the corrosion inside 20th century power lines, the galvanic corrosion of steel and aluminum from 1949 was examined. In this investigation, 0.1 M Na2SO4 + 1 mM NaCl was used as moderately corrosive medium. Various electrochemical methods were applied to determine the corrosion potential and the different reactions involved in the corrosion process. The thickness of the oxide layer that regulates the corrosion of aluminum was obtained from impedance measurement and it was shown that the diffusion of oxygen through a porous oxide layer is the governing stage for the reaction occurring at the steel electrode. Finally, the corrosion of steel regulates the corrosion of both metals when they are in electrical contact.

Keywords: Galvanic corrosion, Steel, Aluminum, EIS, ACSR

Graphical Abstract

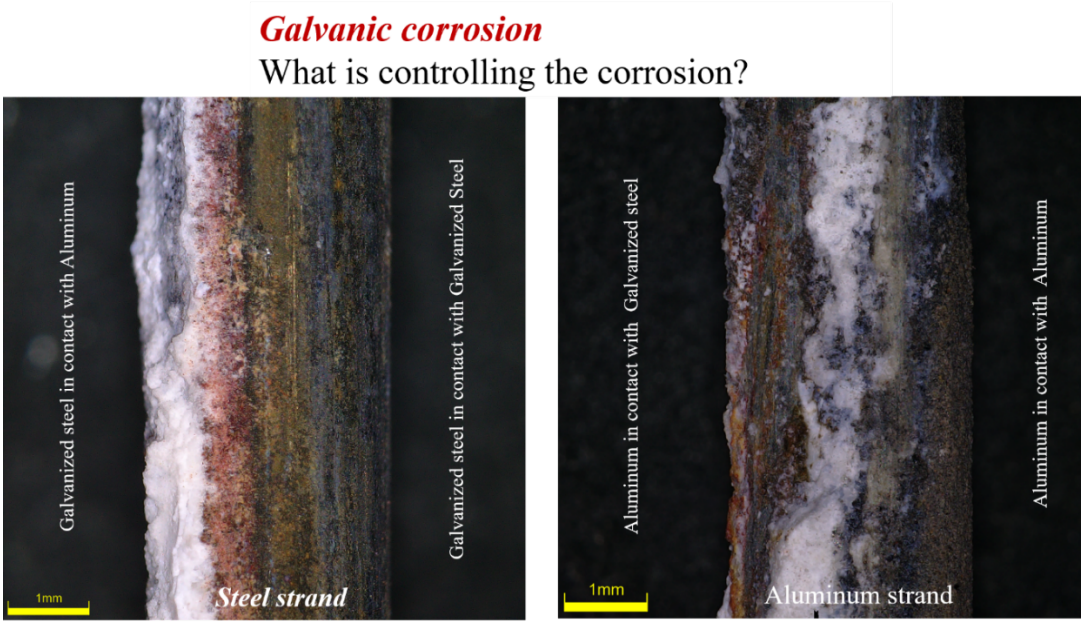

1. Introduction

In rapidly-growing civilizations, it is essential to ensure a constant supply of electricity to all facilities. Maintaining a robust transmission network and understanding the deterioration process within overhead power wires are critical [1-8].

In France, the Réseau de Transport d'Électricité (RTE) is in charge of the transport system, which is made up of cables from various periods, including those dating back to the first half of the 20th century. Certain cables, though older than anticipated, have continued to function for longer than expected. Therefore, it is even more critical to understand the material corrosion process in order to capitalize on these positive outcomes and create new, more robust cable technologies.

During the first part of the 20th century, the majority of overhead power lines were made up of rows of aluminum alloy strands that were grease-coated to protect them and reinforced in the middle by galvanized steel strands. The term "Aluminum Conductor Steel-Reinforced cables" (ACSR) refers to these cables [8].

Iron is expected to be more noble than aluminum based on their respective corrosion potentials. Moreover, the system formed by the ACSR , Figure 1, is complex because it involves three metals, forming different interfaces: steel beneath the zinc layer, zinc from the galvanization film, and aluminum from the aluminum strands [5, 7, 9].

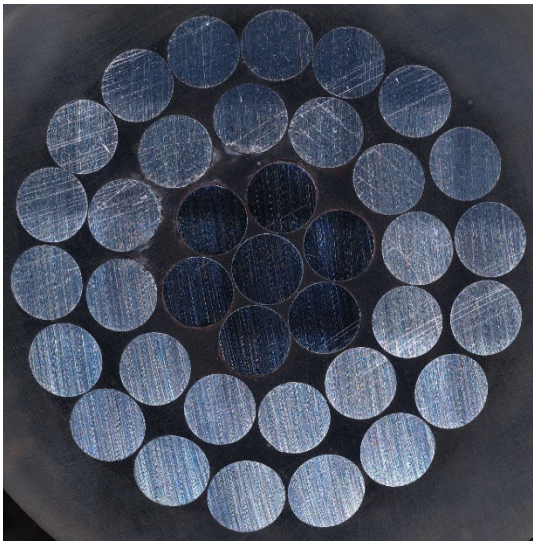

Figure 1.-Aluminum Conductor Steel-Reinforced Cable (ACRS) from CROCUS type conductor dating from 1949 provided by RTE.

After 74 years of operation and environmental exposure, the ACSR shown in Figure 1 has sustained some damage, though not enough to warrant decommissioning. The cables may start galvanic corrosion when they come into mechanical contact without lubricant. As a result, the more noble metal will act as a cathode and the less noble metal as an anode. This means that the more noble metal will corrode more slowly than it would if it were alone, while the less noble metal will corrode faster. For instance, two strands in contact, one steel and one aluminum, observed by optical microscopy are presented in Figure 2. Indeed, zinc is removed from the galvanization layer as a result of the galvanic coupling of Al and Zn, which dissolves zinc forming zinc hydroxide precipitates in high pH zones as a result of reaction (1). Depending on the electrolyte, it can produce the white deposits shown in Figure 2, the composition of which may vary depending on the nature of ions in solution [10-14]. The corrosion of the Al-Steel galvanic pair starts as soon as the zinc layer is consumed. This is demonstrated by the red oxide film that is present in both images of Figure 2.

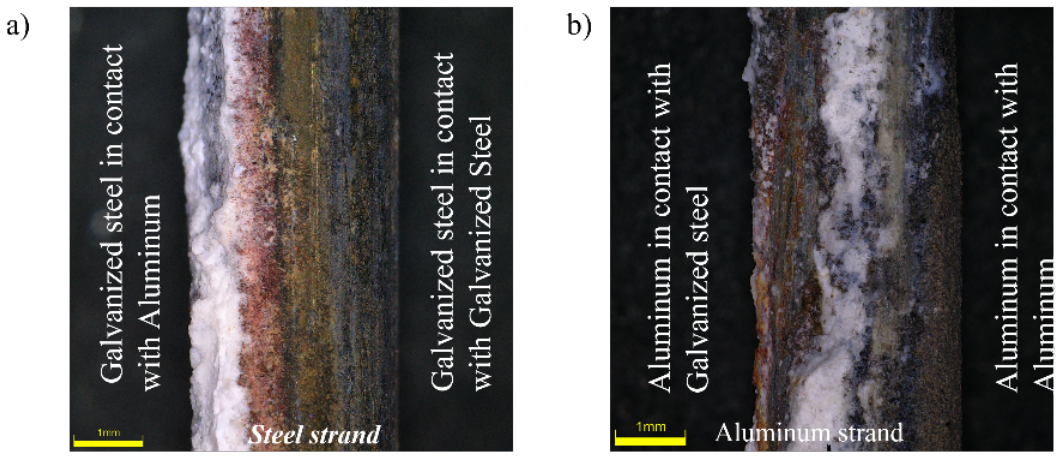

Figure 2.- Optical images of the strands in contact inside the ACSR, (a) galvanized steel strand and (b) aluminum strand.

Steel is expected to experience oxygen reduction as in reaction (1) since aluminum is anodic to steel [15-17]. On the other hand, as in reactions (2) and (3), aluminum dissolves and forms aluminum hydroxides [16-20].

$$O_2 + 2H_2O + 4e^- \rightarrow 4OH^- \quad (1)$$

$$Al + 3OH^- \rightarrow Al(OH)_3 + 3e^- \quad (2)$$

$$Al(OH)_3 + OH^- \rightarrow Al(OH)_4^- \quad (3)$$

However, for pH values between 4 and 10, the passive film on aluminum acts as a barrier layer. It dissolves much slower than outside of this pH range [19], and when steel is in contact with aluminum, steel forms an oxide layer according to reaction (4) [16, 21, 22], thus forming iron (II) hydroxide, which in turn reacts with water and oxygen to form iron oxyhydroxides [23-25].

$$Fe + 2OH^- \rightarrow Fe(OH)_2 + 2e^- \quad (4)$$

Moreover, processes that occur during galvanic corrosion, reactions (1) to (3), cause local pH changes, as well as current and potential distributions [26-31]. This behavior affects not only the rate of corrosion, but also the reactions that can develop in each zone [26, 27, 30-36].

The environment, such as those close to the seaside, has an impact on the corrosion inside ACSR. Additionally, it has been demonstrated that corrosion affects these cables' mechanical qualities, and several methods have been used to estimate how long they will last [1-4, 37, 38].

However, employing electrochemical methods remains to be one of the finest approaches to comprehend the corrosion process [10, 15-17, 26-29, 32-34, 39-43]. Thus, the purpose of this work is to evaluate the aluminum-steel galvanic pair utilizing electrochemical techniques such as corrosion potential monitoring, linear sweep voltammetry, and electrochemical impedance spectroscopy. The second objective of this work was to comprehend the process responsible for the corrosion of these cables in the absence of zinc.

2. Materials

The electrochemical measurements were performed in a 0.1 M Na_2SO_4 (ACROS ORGANICS 99%) and 1 mM NaCl (VWR Chemicals 100%) solution prepared with twice-distilled water (2-6 μS/cm), to simulate an aggressive environment, *i.e.,* sea spray [8].

The aluminum alloy and the steel were taken from an ACSR conductor dating from 1949 from the line Angers-Corbière-Ecouflant supplied by RTE.

As the steel was galvanized, the zinc was removed from the steel by polishing it with 120 SiC paper first, and then immersing it for 30 seconds in a 5% HNO_3 solution to remove the residual zinc. The final process involved polishing the steel with 1200 SiC abrasive paper. In the case of aluminum, pollution from exposure since 1949 and the remnants of the old lubricant have created a black film on the surface. By polishing with SiC abrasive paper ranging in grade from 320 to 1200, this film was removed.

The strands were insulated in an epoxy resin (Buehler EpoxyCure 2), then polished from 320 to 1200 abrasive paper using water and 4000 abrasive paper using 96% ethanol until the surface of interest was exposed. To replicate the aluminum-steel ratio inside the ACSR, three different types of electrodes were created: a single aluminum or steel strand, two strands, one of each strand (2S), and five strands, one steel and four aluminum ones (5S), to simulate the ratio of aluminum-steel inside the ACSR. In every case, the exposed surface was made up of discs, as seen in Figure 1.

For the electrochemical measurements, a BioLogic MPG-200 multi-potentiostat was used. The working electrode consisted of aluminum and steel strands, a saturated mercury sulfate electrode (SSE) was used as a reference electrode, and a platinum mesh was used as a counter electrode. However, all potentials were reported with respect to the saturated calomel electrode (SCE), as it is the most used electrode in corrosion studies. At the same time, to correctly measure impedance at frequencies above 10 kHz, a 100 nF capacitor was soldered to a platinum wire, which was then shorted off and connected to the reference electrode [44].

Three electrochemical techniques were used: the corrosion potential measurement (E_{corr}), the linear sweep voltammetry (LSV), and the electrochemical impedance spectroscopy (EIS). The corrosion potential of each metal was monitored separately in a three-electrode cell for a few days in order to confirm that the aluminum alloy utilized in this work was less noble than the steel.

LSV was used to confirm the corrosion potential of the galvanic pair (2S or 5S). The potential was swept after 2, 24, 48 and 72 hours of immersion from a value close to the corrosion potential ($E_{corr} \pm 0.1\,V$), allowing the anodic and cathodic branches to be measured independently. The intersection of the two curves for steel and aluminum provided the E_{corr} of the galvanic pair, which matches the experimentally measured values (vide infra).

For the EIS, the dc potential was set at E_{corr}, the amplitude of the sine wave perturbation was 10 mV, and the frequency was swept between 100 kHz to 10 mHz with 10 points per frequency decade. These experimental conditions were selected to fulfill linearity and stationarity of the electrochemical system during the EIS measurement. EIS provides information about the thickness of the oxide layer, time constants that may be connected to the limiting step in an electrochemical system, and the state of the surface without destroying it, which is a significant advantage over LSV. The LSV allows the calculation of E_{corr} and the corrosion current density (j_{corr}) [9].

3. Results and discussion

3.1.Corrosion potential and linear sweep voltammetry

For a period of seven days, the corrosion potential (E_{corr}) was monitored for different types of electrodes (Figure 3). With increasing immersion time, the corrosion potential of aluminum (red solid line), becomes nobler with the immersion time and tends towards -0.70 V vs SCE, while after 4 days, E_{corr} for Steel (blue solid line), becomes less noble with time, remaining at about -0.70 V vs SCE. The potential difference between aluminum and steel points out the possibility of galvanic corrosion. Nonetheless, it is important to note that these two curves intersect after 4.5 days, demonstrating polarity inversion during galvanic corrosion [32, 40].

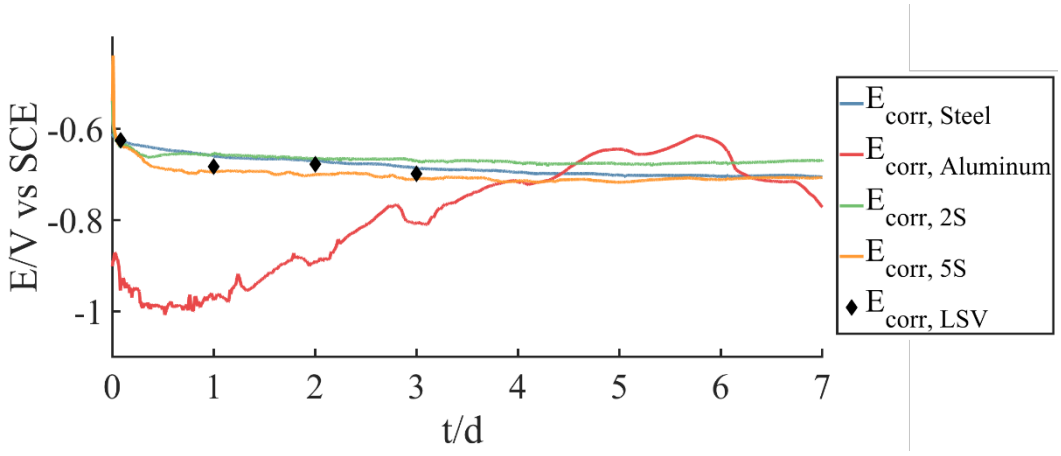

Figure 3.- Corrosion potential (E_{corr}) measured during 72 hours in a 0.1 M Na_2SO_4 + 1 mM NaCl solution for the four types of electrodes: 1 aluminum strand (red solid line), 1 steel strand (blue solid line), 1 aluminum strand in mechanical contact with 1 steel strand (2S green solid line), 4 aluminum

strands in contact with 1 steel strand (5S yellow solid line). E_{corr} predicted by the intercept of polarization curves are shown as diamond markers.

The electrodes 2S (one aluminum strand and one steel strand in mechanical contact) and 5S (four aluminum strands and one steel strand) have different E_{corr} values which are represented by the green and yellow curves, respectively. After seven days, all corrosion potentials tend towards -0.70 V versus SCE, which helps to explain why these materials did not corrode quickly. In both situations, the potential is becoming less noble with time.

LSV was carried out after various immersion times for single aluminum and steel electrodes, as shown in Figure 4.

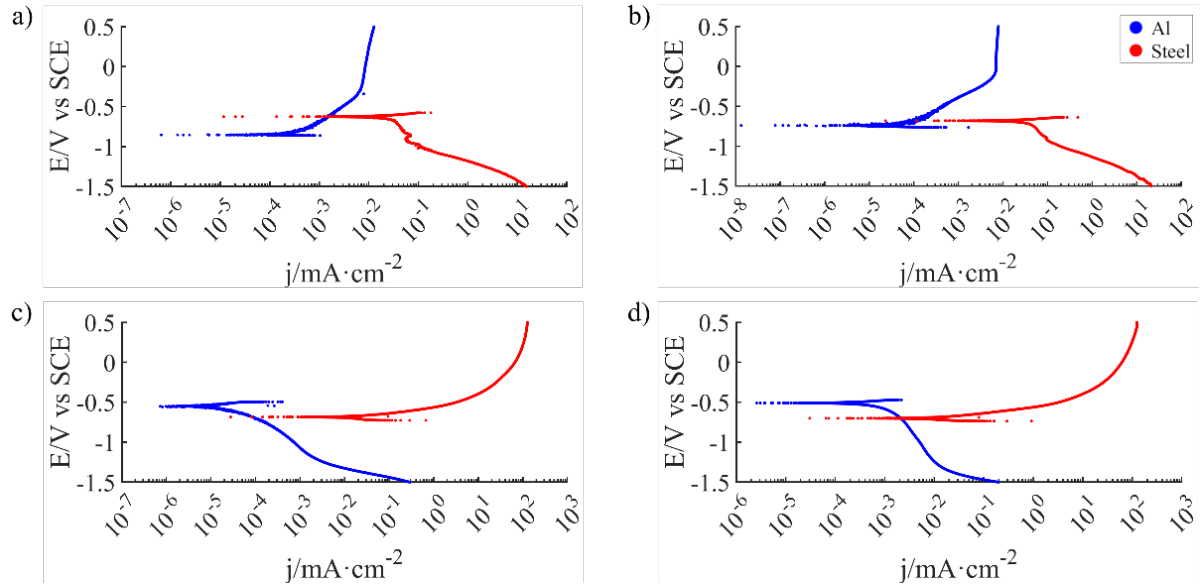

Figure 4.- Polarization curves (LSV) for aluminum (blue) and Steel (red) for (a) 2, (b) 24, (c) 48 and (d) 72 hours of immersion in a 0.1 M Na_2SO_4 + 1 mM NaCl solution, potential swept at 1mV/s.

During the first 24 hours of immersion, the intercept of the LSV curves for aluminum and steel occurs on the anodic branch of aluminum, which exhibits the usual behavior for aluminum [18-20, 45-47] showing the behavior of aluminum in this domain. However, after 48 hours of immersion, the intercept happens on the cathodic branch of the aluminum LSV, between -0.90 and -1.20 V/SCE, *i.e.*, matching the oxygen reduction domain [35, 48].

E_{corr} can be inferred from the intercept of the LSV curves, and was plotted in Figure 3 as black symbols. It closely follows the curve obtained for the 2S and 5S electrodes (yellow and green lines in Figure 3).

3.2.Electrochemical Impedance Spectroscopy: Aluminum alloy

Each material was characterized separately. Initially, aluminum corrosion was observed for seven days to use EIS to track the growth of the oxide film [49-54]. These data are shown in Figure 5. After 1 and 2 days of immersion, Figure 5a, the Nyquist diagrams show two capacitive loops. In contrast, over three days or longer of immersion, only the beginning of a single capacitive loop can be observed. A close examination of the imaginary part of the impedance as a function of the frequency, Figure 5c, shows that the aluminum passivation is strengthened. This is characterized by an increasing total impedance with an increase in immersion duration.

From the evolution of the phase as a function of the frequency presented in Figure 5d, which shows the corrected EIS data for the uncompensated electrolyte resistance [50-55], a constant phase element (CPE), which is equivalent to a divergence from the predicted plateau at 90°, can be seen. A plateau is seen after one day of immersion, ranging from 1 kHz to about 1 Hz; however, the plateau's extension increases with immersion time. Immersed for seven days, its frequency range spans from 1 kHz to 100 mHz. As reported elsewhere, the Constant Phase Element (CPE) parameters accounting for the double layer can be obtained from a graphical EIS data analysis [51, 52, 54].

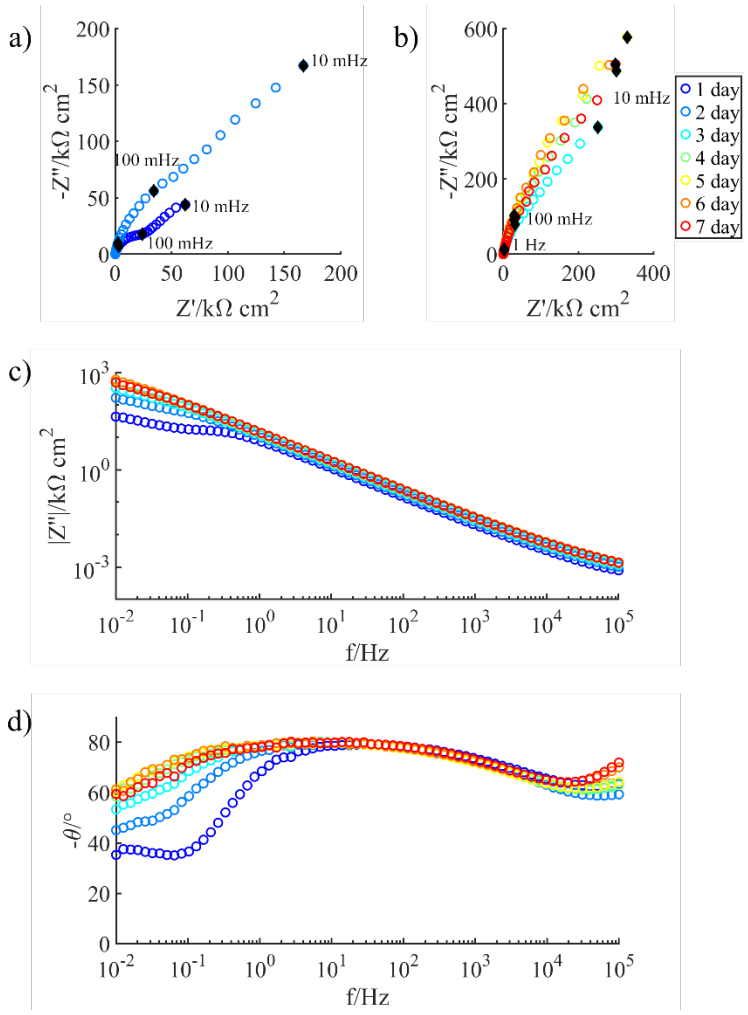

Figure 5.- (a) Nyquist diagrams for 1 and 2 days of immersion, (b) Nyquist diagrams for 3 to 7 days of immersion, (c) Bode diagram of the imaginary part, and (d) Bode phase diagram for an aluminum strand obtained every 24 hours during 7 days of immersion in 0.1 M Na_2SO_4 + 1 mM NaCl, 10 points per decade, 10 mV amplitude and $E_{dc} = OCP$

Furthermore, by carefully examining these EIS diagrams, the oxide film's thickness can be determined [49, 51, 52] by correcting the impedance due to double layer capacitance using Equation 1, where Z_{cor} is the corrected impedance from the electrolyte resistance, Z_{exp} the experimental impedance, j the imaginary number, ω the angular frequency, α_{dl} the exponent obtained the first slope of Figure 5c (between 10 kHz and 1 Hz), and Q_{dl} can be obtained in the low-frequency domain as developed by Gharbi et al.[51]. This corrected impedance is then used to calculate the complex capacitance using Equation 2, in which C is the complex capacitance. From the values at high frequencies, it is possible to extrapolate the value of the static capacitance, C_∞, which in this case corresponds to the capacitance of the oxide layer,

C_{ox}. This value is, in turn, used to calculate the thickness of the passive film using Equation 3, where ε_0 is the vacuum permittivity, ε the permittivity of aluminum oxide ($\varepsilon = 11.5$) and δ the thickness of the passive layer.

$$Z_{cor} = Z_{exp} - \frac{1}{(j\omega)^{\alpha_{dl}} Q_{dl}} \quad \text{Equation 1}$$

$$C = \frac{1}{j\omega[Z_{cor} - R_e]} \quad \text{Equation 2}$$

$$C_\infty = C_{ox} = \frac{\varepsilon_0 \varepsilon}{\delta} \quad \text{Equation 3}$$

The evolution of the oxide film thickness is shown in Figure 6. The value rises asymptotically with time, and after four days of immersion, it reaches a value of about 9 nm, which agrees with previously reported data [49-51]. Furthermore, the increase in passive film thickness can account for the rise in impedance amplitude with immersion time.

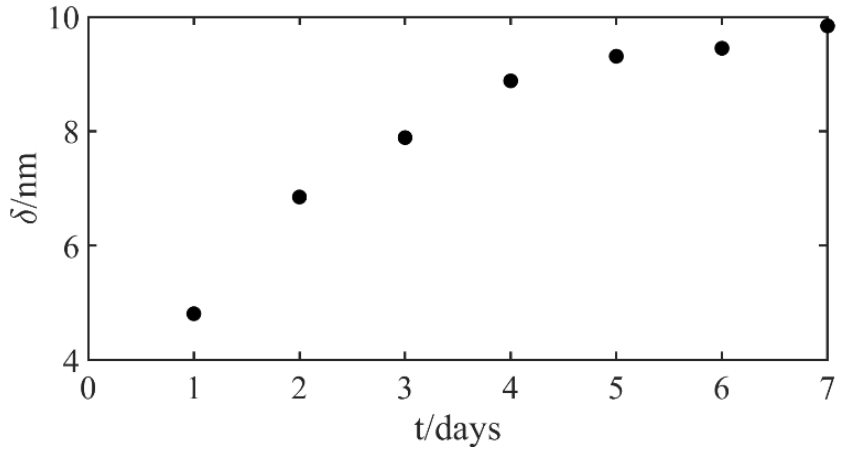

Figure 6.- Evolution of film thickness calculated from the EIS data in Figure 5 for an aluminum strand in 0.1 M Na_2SO_4 + 1 mM NaCl at the OCP.

3.3.Electrochemical Impedance Spectroscopy: Steel

Steel corrosion was also monitored using EIS. The Nyquist diagram is shown in Figure 7 for immersion times ranging from 1 to 7 days.

A linear domain is shown in Figure 7a. The phase angle is reported for each dotted line, and decreases in size with immersion time. After 7 seven days of immersion, it reaches 29.7, as

shown in Figure 7a for frequencies over 1 kHz. The low-frequency capacitive loop, Figure 7b, is observed for all immersion times, and its amplitude increases with time. Such a behavior points out to the formation of a porous layer (see below). As a result, it was decided that applying the geometric area to normalize the data would be misleading.

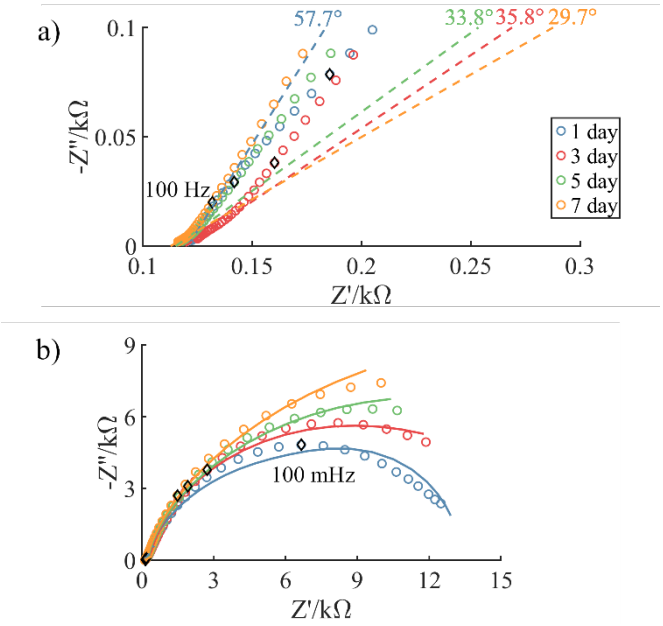

Figure 7.- (a) Nyquist diagrams, (b) Nyquist diagrams at high frequencies, and () Bode phase diagram for 1 (blue), 3 (red), 5 (green), and 7 (yellow) days of immersion in 0.1 M Na_2SO_4 + 1 mM NaCl at the OCP, the symbols are the experimental data, the solid lines are the fitting of the experimental data, the dotted line indicates the angle of the high frequency and the black symbols represent 100 Hz and 100 mHz as indicated in the figure.

The shape of the Nyquist diagrams can be explained by the presence of a porous oxide layer over the steel surface, as previously shown by Frateur et al.[56-58] in the case of the corrosion of cast iron in drinking water. Observation of the steel working electrode after seven days of immersion with an optical microscope shows great similarity with the results by Frateur et al. [58] (see Supplementary Material). The red oxide layer is electronically insulating and ionically conductive, while the black oxide layer has opposite characteristics. Additionally, the black oxide layer is covered by a porous "green rust" [56-58].

The de Levie impedance, Equation 4, can be used to describe the oxygen reduction reaction, which is the cathodic reaction on steel, for which the impedance of a pore is expressed by Equation 4 [56-59], which accounts for R_0, the ohmic drop inside the pore for a unit length of the pore ($\Omega\ cm^{-1}$). This parameter is directly proportional to the resistivity of the solution, ρ

(Ω cm) and inversely proportional to the square of the radius of the pore, r (cm). Z_0, the interfacial impedance (also considered for a unit length of the pore - Ω cm), is represented by the equivalent circuit presented in Figure 8a, which consists of a parallel *RC* arrangement identified by the subscript *f* representing the ohmic drop inside the "green rust", in series with a Randles-type circuit modified for finite diffusion, Z_D. This finite diffusion is given by the by Equation 6. Finally, L is the length of the pore in cm. Since $Z_{deLevie}$ accounts for the impedance of a single pore, the whole cathodic impedance, Z_C, is expressed for N pores in Equation 7.

Both the anodic and cathodic reactions are in equilibrium as the corrosion of steel is studied at the corrosion potential. Consequently, the equivalent circuit representing the whole system, Figure 8b, must account for two parallel impedances, Z_A and Z_C, where Z_A is the anodic impedance given by the equivalent circuit in Figure 8c, and Z_C is the cathodic impedance represents all the pores on the surface of steel and is given by Equation 7.

The analogous circuit shown in Figure 8b provides the total impedance for the corrosion of steel. Z_C and Z_A are connected in parallel to indicate the simultaneous occurrence of both reactions, while the solution resistance R_e, is connected in series.

Several simplifications were made to make fitting the impedance data easier. First, time constants were used in place of capacitances (Equation 8)[57]. The pore length (L), number of pores (N), and pore radius (r) are also included in the de Levie formula. As a result, only the ratio of pore length to pore radius (L/r) (Equation 9) and the product of pore number and pore radius (rN) (Equation 10) can be calculated.

$$Z_{deLevie} = \sqrt{R_0 Z_0}\coth\left(L\sqrt{\frac{R_0}{Z_0}}\right) \qquad \text{Equation 4}$$

$$R_0 = \frac{\rho}{\pi r^2} \qquad \text{Equation 5}$$

$$Z_D = R_D\frac{\tanh\sqrt{j\omega\tau_D}}{\sqrt{j\omega\tau_D}} \qquad \text{Equation 6}$$

$$Z_C = \frac{Z_{deLevie}}{N}$$ Equation 7

$$\tau_i \equiv C_i R_i$$ Equation 8

$$R_L = R_0 L^2 = \frac{\rho}{\pi}\frac{L^2}{r^2}$$ Equation 9

$$R_N = \frac{R_0}{N^2} = \frac{\rho}{\pi}\frac{1}{r^2 N^2}$$ Equation 10

The fitting of the data was performed with the Measurement Model program [60]. The fitting of the experimental data with the equivalent circuit is presented as a solid line in Figure 7, showing a good agreement between these results and the corrosion process description.

Figure 9 shows the time constants and the link between the characteristic dimensions of the pore. The time constants for diffusion, the cathodic reaction, the anodic reaction and the ohmic drop in the "green rust" (τ_D, τ_C, τ_A, and τ_f) are shown in Figure 9a. For all the cases, the time constant increases with the immersion time increases, indicating that corrosion processes are progressively slower.

It can be seen that the highest time constant is τ_D. This suggests that corrosion of steel is controlled by oxygen diffusion through the macropores formed by the black oxide. Let us remember that τ_D is directly proportional to the thickness of the diffusion layer (Equation 11). Since the diffusion coefficient is time-independent, these changes must be ascribed to a change in the thickness of the diffusion layer, i.e., an increase in the oxide layer.

$$\tau_D = \frac{\delta^2}{D_{Ox}}$$ Equation 11

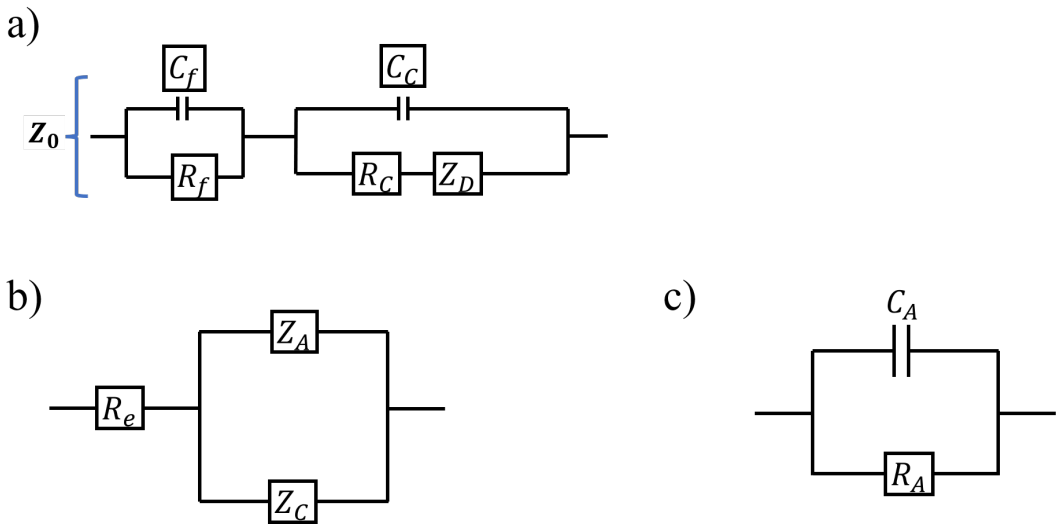

Figure 8.- Equivalent circuits of (a) interfacial impedance inside a pore, (b) complete impedance with an anodic and a cathodic branch and (c) the anodic impedance.

The characteristic dimensions of the pore are its length, radius and quantity of pores (*L, r, and N*). Two of these values can be obtained from the fitting of the experimental results, *L/r* and *Nr*, which are shown in Figure 9b [56]. After the first day of immersion, *rN* drops significantly, then increases and stabilizes after the fifth day of immersion; *L*/r increases over the first four days of immersion, then steadily decreases. We can therefore conclude that r decreases on the first and second immersion days, increasing *L/r* and decreasing *Nr*; these two values increase on the second and fourth immersion days. If *r* continues to decrese, this could account for the increase of *L/r*; on the other hand, *Nr* should decrease, which is not the case; this could be explained by an increase of the number of pores, *N*.

After five days of immersion, *L/r* finally decreases slightly while Nr tends to six. Frateur et al. noted that r diminishes asymptotically [57, 58] which helps to explain why *Nr* tends to a constant value then *L/r* gradually decreases between the fifth and seventh day. his could be due to the porous oxide layer slowly dissolving.

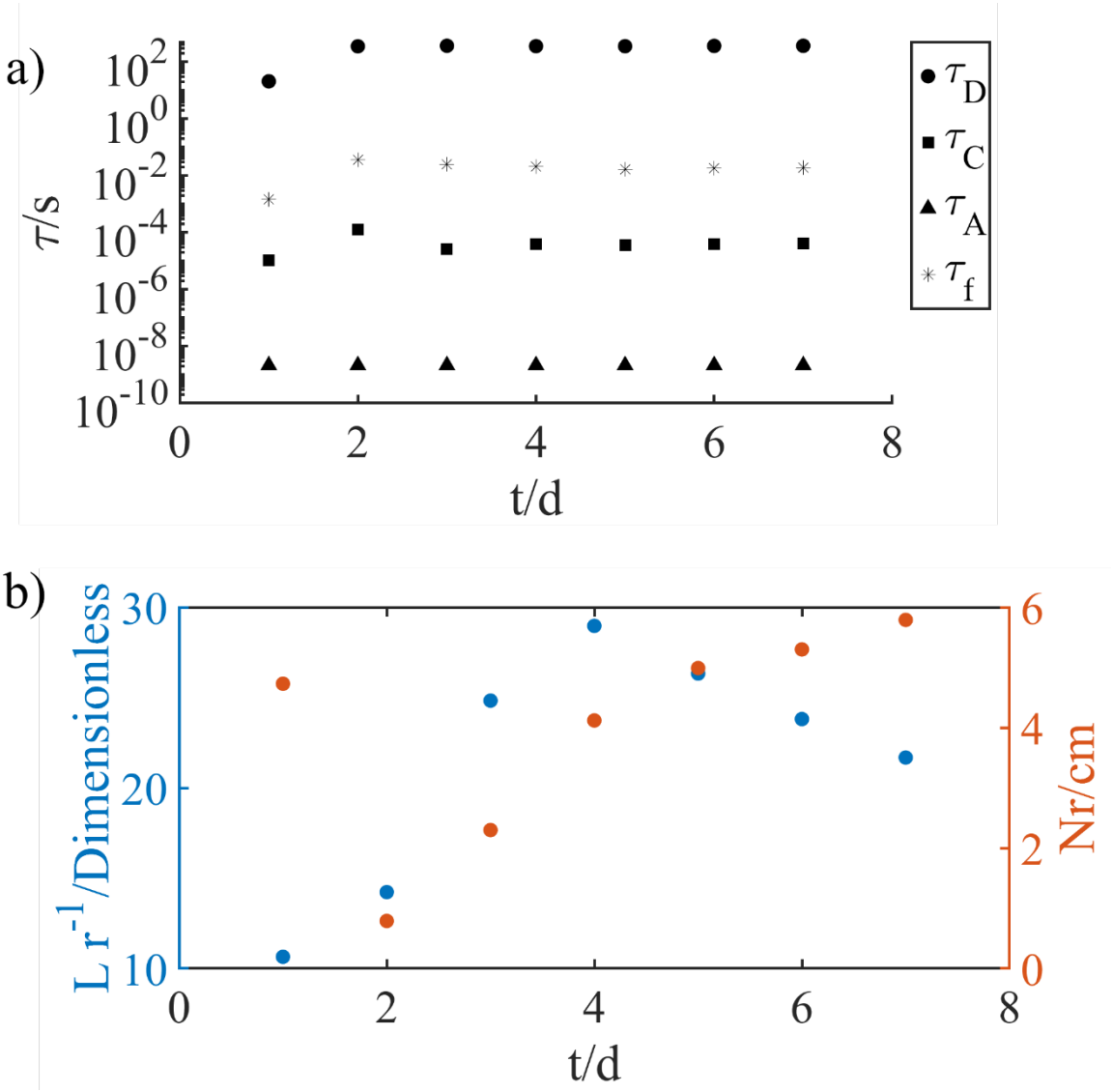

Figure 9.- (a) Time constants, and (b) relationship of the dimensions of a pore and quantity of pores obtained from the fitting using the equivalent circuit in Figure 8b.

3.4.Electrochemical Impedance Spectroscopy: Galvanic Pair Al-Steel

The corrosion of the galvanic pair was studied using the same experimental procedure. The EIS spectra are shown in Figure 10, the color gradient indicates the immersion time, except for Figure 10d which shows the evolution of the phase in the high-frequency domain for 1

day (blue circles) and 30 days of immersion (red circles), the dotted line represents the angle of inclination of the linear zone.

The Nyquist diagrams presented in Figure 10a show a flat capacitive loop in the low frequency domain, similar to the one observed for steel (Figure 7b), and a small flat capacitive loop follow by a linear domain is observed in the high-frequency domain (Figure 10b). As the immersion time increases the amplitude of the impedance decreases. It is interesting to note that even though there are two strands for these experiments, the impedance response of the system after one day of immersion, and especially the low frequency limit, is similar to the results obtained for a single strand of steel.

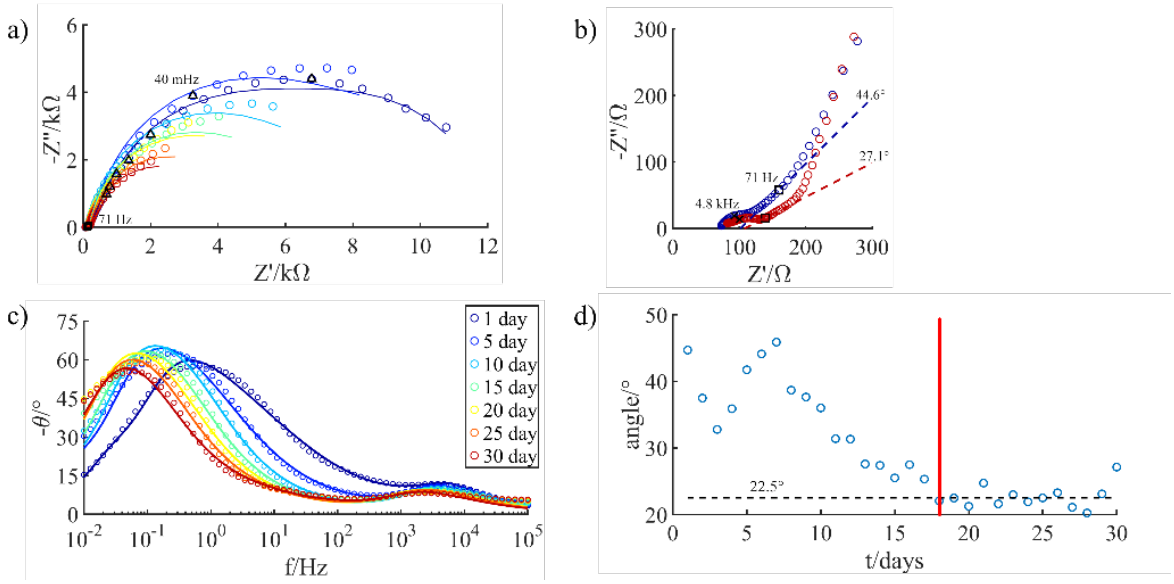

Figure 10.- (a) Nyquist diagram, (b) Nyquist diagram of the high-frequency domain indicating the angles of the linear zone, (c) Bode phase diagram, and (d) evolution of the angle of the linear zone in the high-frequency domain for different immersion times in 0.1 M Na_2SO_4 + 1 mM NaCl, the symbols are the experimental data, the solid lines are the fitting of the experimental data, the dotted line indicates the angle of the high frequency and the black symbols represent specific frequencies indicated in the figure.

During the first 5 days of immersion, the impedance slightly increases, as can be seen from the low-frequency domain. This trend indicates the passivation of the surface; however, the impedance begins to diminish after the immersion period of five days or more (Figure 10a).

Figure 10b shows the high-frequency domain of the Nyquist diagram after one day of immersion (blue circles) and 30 days of immersion (red circles). The high-frequency domain

consists of a flattened capacitive loop and a linear domain with a phase angle of 44.6° and 27.1°, respectively. This change in the phase angle is better seen in Figure 10c in the frequency domain between 5 and 1000 Hz.

This behavior of the EIS response can be explained in a similar way to that of steel corrosion. Steel is covered by a red oxide layer, and underneath, a black oxide layer similar to that of steel is observed; this is illustrated in the Supplementary Material.

The impedance to this system can be represented as in Figure 8b: where Z_A will account for the anodic reactions on both the steel and the aluminum, and Z_C takes into account the reduction of oxygen occurring in the porous layer formed by the iron oxides on steel.

The fitted data are presented as solid lines in Figure 10a and c. As with steel, the ratio between pore length and radius (*L/*r) and the ratio between pore radius and number of pores (*rN*) are shown in blue and orange respectively in Figure 11a. *L/*r remains around 6 and after 15 days of immersion, starts to increase similarly to the behavior observed in Figure 10d where the angle indicates that after 17 days of immersion (marked by a red line), the system behaves as a semi-infinite porous layer which corresponds to a ratio *L/*r of 8.

On the other hand, the *Nr* parameter, shown in orange in Figure 11, fluctuates during the first seven days, similar to the inclination of the linear zone as seen in Figure 10d over the same period. After the seventh day of immersion, it remains constant until the 21st day of immersion, after which it decreases and tends towards 1.

During the first three days of immersion, *L/r* rises sharply while *Nr* drops. This behavior mirrors the observed pattern for steel, suggesting a reduction in *r*. After the fourth day, *L/r* remains approximately at 5 while *Nr* fluctuates around 2 until the tenth day. This could imply that *L* and *r* remain constant while *N* changes, potentially due to the protective effects of aluminum, such as aluminum dissolution. Subsequently, after the tenth day, *L/r* begins to increase while *Nr* stabilizes. This could be attributed to an increase in *L* and *N* alongside a decrease in *r*. Finally, after the twentieth day of immersion, *L/r* continues to increase while *Nr* decreases. This suggests that *N* stops to increase while *r* continues to decrease.

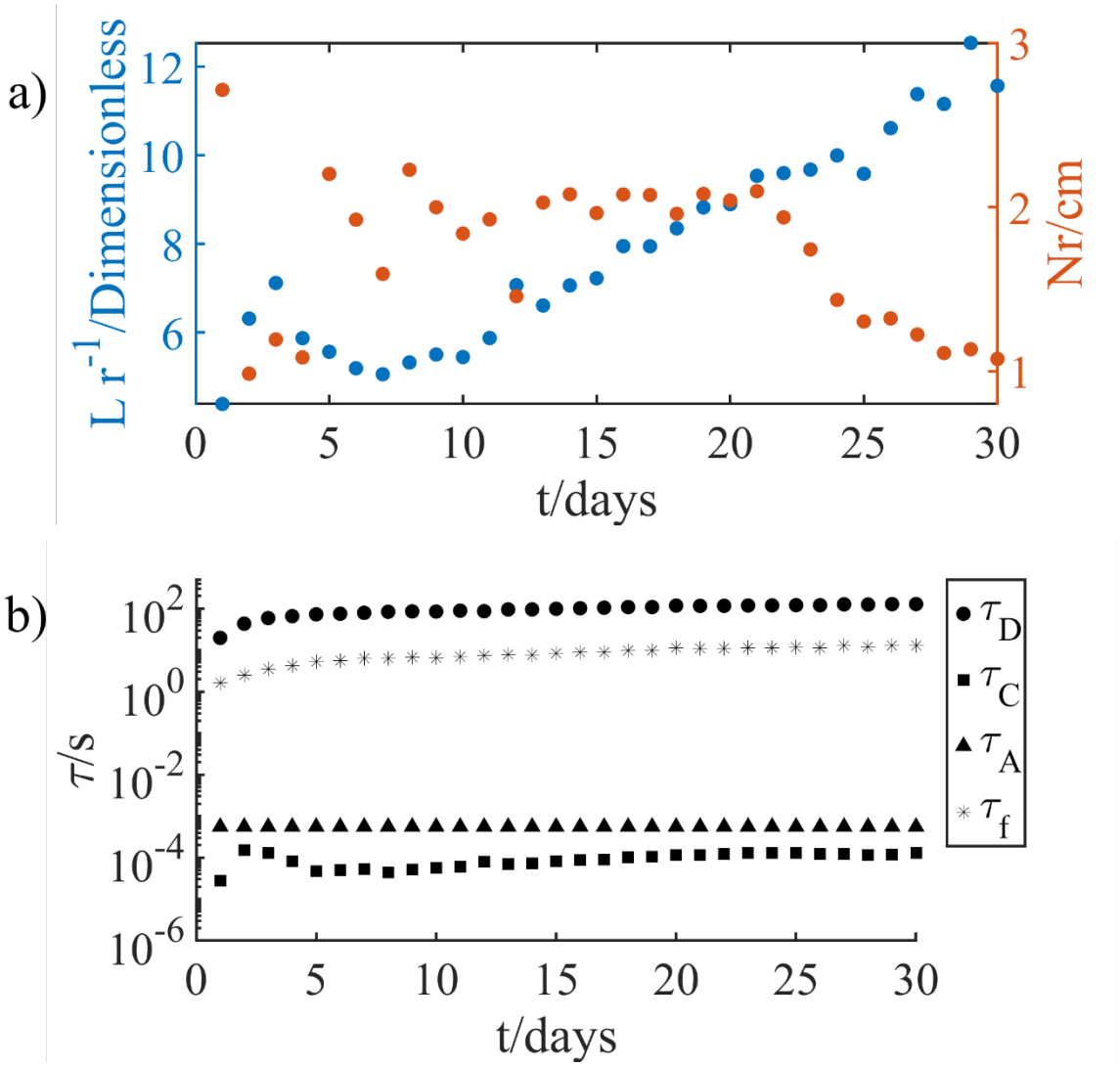

Figure 11.- Evolution of (a) the ratio of the length of the pore and its radius (blue) and the relation between the radius and the number of pores (orange), and (b) time constants obtained from fitting the data for the 2S sample.

The time constants obtained from the result of the fitting are presented in Figure 11b. Similar to the case for steel, τ_D is the biggest time constat, this time constant is at the same magnitude than for steel. It is possible to conclude that the diffusion of oxygen is the controlling step for the galvanic pair's corrosion. As it was mentioned previously, τ_D can be expressed by Equation 11. If we assume that the diffusion coefficient is independent of time [61], the increase in the time constant must be attributed to an increase in the thickness of the diffusion layer (*i.e.*, the oxide layer).

The behavior is the opposite of that described by Frateur et al. [58], where the lower time constant belongs to the green rust layer, in the case of the time constants for the cathodic reaction and the ohmic drop in the green rust layer. Aluminum may be the cause of this behavior if it alters the local pH, potential, and current distribution at the surface. Similar observations were reported by Van Nam Tran et al. in 2020 using 6061-T6 aluminum alloy and high-strength steel [62]. As was noted in this paper, the impedance of the galvanic couple was between the impedances of the metals corroding separately (see Supplementary Material). However, aluminum seemed to be more active in their situation. This could be attributed to the concentration of chlorides since they used concentration of 400 mM or more [63].

From the time constant defined in Equation 8, it is possible to calculate de capacitance ascribed to the "green rust", C_f (Figure 12). Equation 3 shows that the impedance is inversely proportional to the thickness of the oxide layer. Consequently, if C_f for steel (blue dots) and 2S (red dots) it is possible to expect the thickness of the "green rust" on the surface of 2S to be bigger than the one on steel. However, this conclusion should be taken with reservations since the real area is unknown at a porous layer [64, 65].

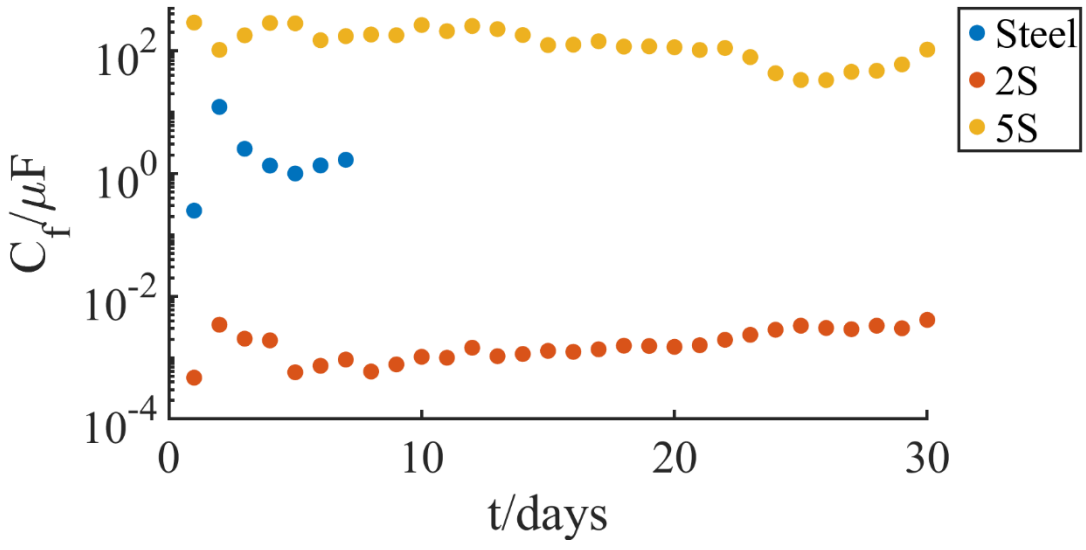

Figure 12.- Evolution of the capacitance of the "green rust" film for steel (blue dots), two strands sample 2S (red dots), and five strands sample 5S (yellow dots).

3.5.Effect of the surface ratio

In the ACSR shown in Figure 1, the surface ratio of steel to aluminum is roughly 0.23 (seven steel strands and thirty aluminum strands). To approximate this ratio, one steel strand was brought into contact with four aluminum strands (sample 5S). The evolution of the corrosion potential (Figure 13) shows that $E_{corr,2S}$ is slightly nobler than $E_{corr,5S}$. The difference is roughly 40 mV for the first 15 days, and decreases to 15 mV after 30 days, which is still quite low for the duration of the immersion.

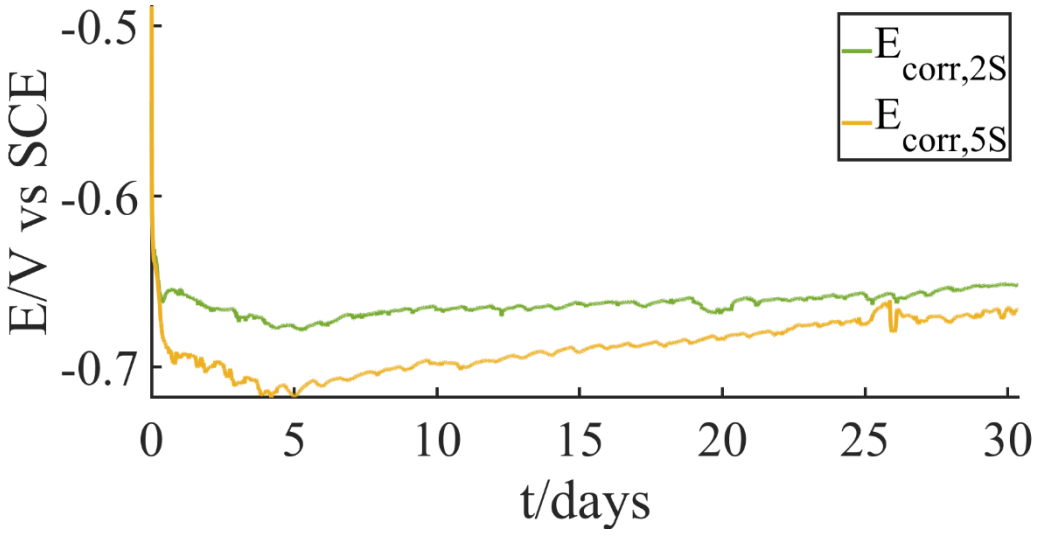

Figure 13.- E_{corr} for 2S (green solid line) and 5S (yellow solid line) in 0.1 M Na_2SO_4 + 1 mM NaCl.

In Figure 14, the Nyquist diagrams for the corrosion of the 5S sample for 30 days of immersion are presented, with measurements performed every 24 hours. Comparable features to the sample with only two strands (Figure 10) can be seen in the spectra, which show a flattened capacitive loop in the low-frequency domain (Figure 14a) and a capacitive loop in the high-frequency domain followed by a linear domain attributed to diffusion in a porous layer (Figure 14b). After 30 days of immersion, the phase angle of the linear zone tends toward 34° (Figure 14c), showing a significant departure from the case for 2S.

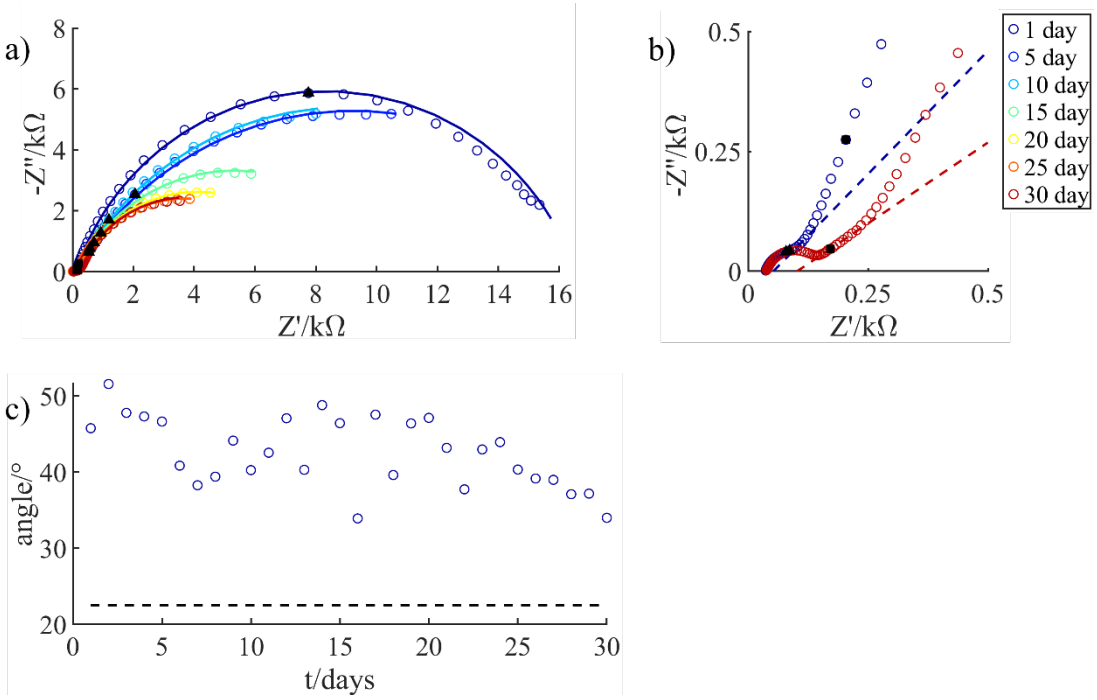

Figure 14.- (a) Nyquist diagram, (b) zoom in the high-frequency domain, and (c) evolution of the phase angle of the linear domain for different immersion times in 0.1 M Na_2SO_4 + 1 mM NaCl at the OCP, the symbols are the experimental data, the solid lines are the fitting of the experimental data, the dotted line indicates the angle of the high frequency and the black symbols represent specific frequencies indicated in the figure.

Moreover, the angle of the linear zone decreases more slowly for 5S (Figure 14c) than for 2S (Figure 10a) and never reaches the theoretical 22.5° that is expected for the diffusion in a semi-infinite porous layer.

To compare the Nyquist diagrams for 2S and 5S, the values have been normalized to the maximum real impedance value, as shown in Figure 15.

For the first day of immersion, the low frequencies of both spectra Figure 15a behave similarly. However, the shift in the position of the red symbols, marking each frequency decade, indicates that the corrosion process for 5S is slower than for 2S, which is logical due to the increased amount of aluminum protecting the steel from corroding faster. In the high-frequency range, as shown in Figure 15b, the capacitive loop is less flattened for 5S than for 2S, and the linear domain around 100 Hz for 2S is less apparent for 5S, which could be due to differences in the porous layer for the two systems.

After 30 days of immersion (Figure 15c), impedance in the low-frequency range behaves similarly for both samples. However, the high-frequency domain clearly shows that the EIS response is by far less flattened for 5S than for 2S (Figure 13d), in agreement with the interpretation of the formation of a porous layer at the electrode surface. This result illustrates the importance of the anode-to-cathode surface ratio for corrosion.

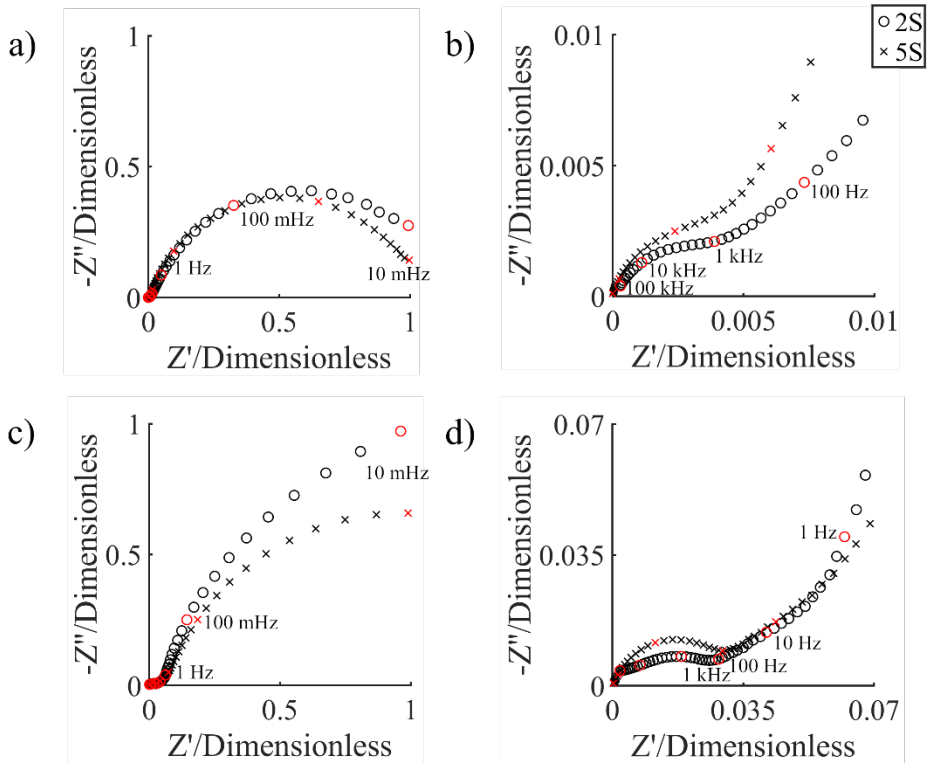

F*igure 15.- Normalized Nyquist diagrams for 2S (circles) and 5S (*crosses*) after (a) 1 day of immersion and (c) 30 days of immersion, and zoom in the high-frequency domain (b and d). The red symbols mark each frequency decade*

To consider the different behaviors of the materials, it is necessary to modify the interfacial impedance of the pore, Z_0. The new equivalent circuit is presented in Figure 16. It consists of a parallel connection of Constant Phase Element (CPE) and resistor, in series with a capacitor-resistor (*RC*) parallel connection. The *CPER*$_f$connection represents the ohmic drop through the "green rust" and the *RC* connection represents the ORR on the black oxide.

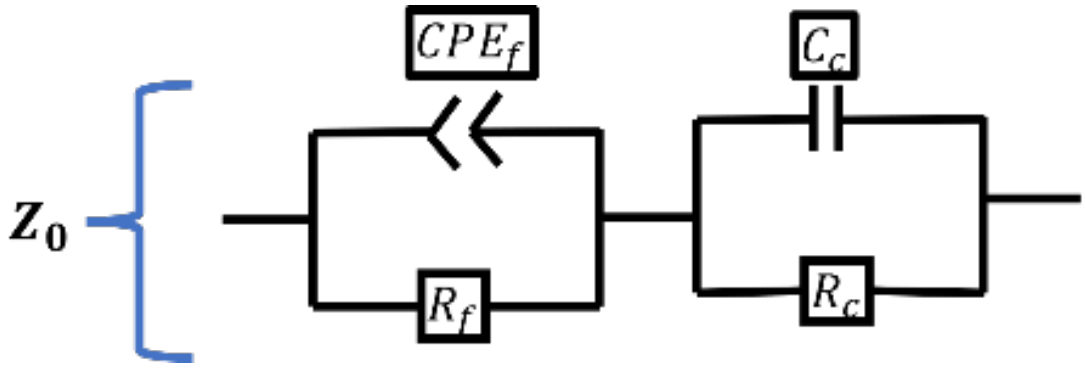

Figure 16.- Equivalent circuits of the interfacial impedance inside a pore for the 5S electrode in 0.1 M Na_2SO_4 + 0.1 M NaCl.

From the fitting of the experimental data, a relationship between the length of the pores and their radius (*L/r*) and the radius and number of pores (*Nr*) can be obtained (Figure 17a). It is evident from Figure 17a that both values increase with the immersion time. After the 22 days of immersion, a sharp increase of *L/r* is followed by a decrease after the 26 days of immersion. If *r* behaves as proposed by Frateur et al. [57, 58], then the increase of *L/r* is likely due to an increase of *L*. On the other hand, the behavior of *Nr* should be attributed to the increase of the number of pores. All in all, this behavior corresponds to an increase in the porosity of the layer.

Figure 17b compiles the time constants for the anodic reaction τ_a, τ_c, and τ_f obtained from the fitting of the EIS experiments performed on sample 5S. Unlike in the case 2S, τ_a is not constant. Its value increases during the first 10 days of immersion, stabilizing at around 2.5 ks, and then rapidly increases after 25 days of immersion, corresponding to the rapid increment of *L/r* and *Nr*. τ_c decreases after the first five days of immersion and remains at about 276 μs for the last part of the immersion period, indicating that the nature of the oxide film does not change over time. τ_f increases steadily for 2S, whereas for 5S, it decreases from the first to the second day of immersion, and afterwards, it increases until it remains nearly constant after five days of immersion. It is possible to calculate the capacitance related to this time constant as shown in Figure 12 (yellow dots). As mentioned previously, the capacitance is inversely proportional to the thickness of the oxide layer. Therefore, in comparison to steel and 2S, it is expected that the green rust would be several times larger

for 5S. However, as the actual surface area is unknown, this result should be regarded cautiously. Furthermore, it is conceivable that the true oxide layer surface area for 5S is greater than that for 2S given the behavior of *L/r*.

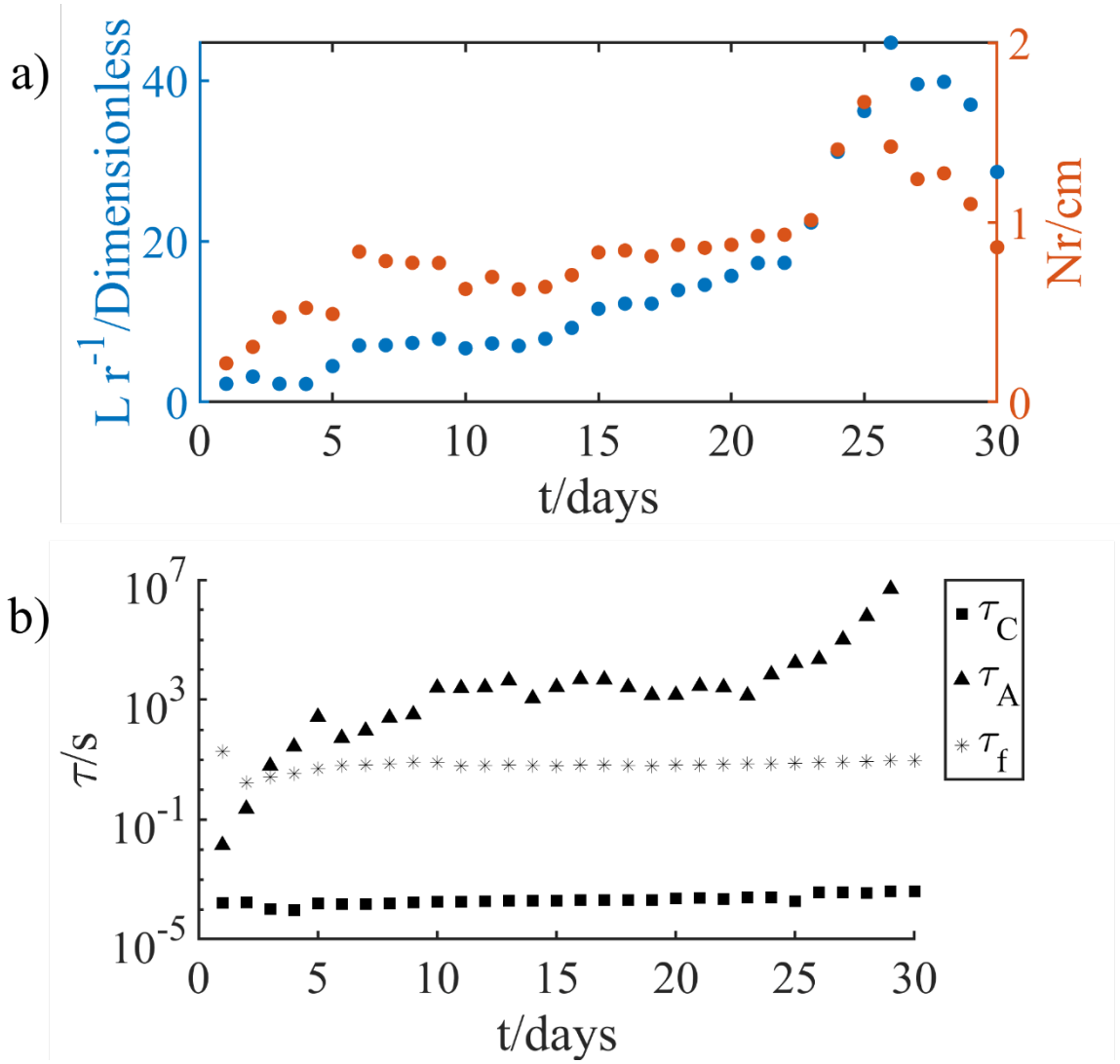

Figure 17.- Evolution of (a) the ratio of the length of the pore and its radius (blue) and the relation between the radius and the number of pores (orange), and (b) time constants obtained from fitting the data for the 5S sample.

4. Discussion

Different electrochemical techniques were used in this work to study the corrosion aged overhead cables: the corrosion potential (E_{corr}) measurement, the linear sweep voltammetry

(LSV), and the electrochemical impedance spectroscopy (EIS). Each provided valuable insights into the corrosion behavior of the galvanic pair Aluminum-Steel.

Firstly, the corrosion potential of steel (Figure 3) is not sufficient to indicate with a good accuracy the passivation of steel. However, the LSV curves (Figure 4) suggested a gradual passivation of the surface (see Supplementary Material), which is also supported by the increase in magnitude of the EIS spectra (Figure 7). Furthermore, the characteristics of the EIS spectra indicated that corrosion is primarily controlled by diffusion within a porous layer. Such a behavior of a porous layer by impedance spectroscopy has been well-studied theoretically [59, 66] and experimentally, on steel [56-58], but also in other systems like porous gold electrodes [67], thus allowing a fine description of the corrosion process involved for these wires.

Secondly, the corrosion potential of aluminum (Figure 3) shows the passivation of the surface as E_{corr} became nobler with the immersion time. This result is in agreement with the LSV curves presented in Figure 4 and EIS spectra presented in Figure 5. The formation of passive film over aluminum has been extensively studied [6, 68-72], and the use of EIS has yielded results consistent with the literature [49-51, 54].

Thirdly, the corrosion potential of the pair Aluminum-Steel (Figure 13) suggested the passivation of the system, supported by the value of E_{corr} predicted from the LSV. Despite the decrease of EIS magnitude over time (Figure 10 and Figure 14), which could be wrongly interpreted as exacerbated corrosion, this reduction was granted to the growth of the porous layer. This conclusion was also supported by the evolution of parameters, L/r, and Nr (Figure 11 and Figure 17).

Inside ACSR, steel was shown to form oxides [73], in agreement with our observations. In the literature, aluminum is said to be less noble than steel [73-79] which was also observed here, but the corrosion of steel during galvanic corrosion was not explained as extensively as in this work. This can be explained by the dissolution of the passive film on aluminum due to a low pH [19, 80, 81] or due to chlorides that help the complexation of $Al(OH)_3$ [62, 63, 68, 69, 81-83].

Xavier and Nishimura studied the galvanic pair Al-Fe in 0.1 M NaCl using the Scanning Electrochemical Microscope (SECM) [76]. Interestingly, they were able to detect Fe^{2+}, Al^{3+} and O_2. They observed the dissolution of iron far from aluminum when both metals are in

contact and the dissolution of aluminum near the boundary between Al and Fe, which is the reason why the authors concluded that Al protects Fe. They were also able to detect O_2 through competition mode of the SECM, allowing to show that oxygen is reduced on the iron part of the metallic assembly. These observations explain why, in our experiments, the zone where aluminum is more attacked is close to steel (see Supplementary Material).

5. Conclusions

The corrosion of steel, aluminum, and the galvanic pair was studied using various electrochemical techniques to identify the controlling step and gain insight into the corrosion of the galvanic pair of steel-aluminum inside a 1949 ACSR cable.

The behavior of the corrosion potential of aluminum suggests surface passivation, whereas the impedance data made it possible to calculate the thickness of the oxide layer, revealing an asymptotic growth of this layer.

When addressing steel, however, the situation becomes more intricate when employing direct current techniques. In such scenarios, EIS emerges as a valuable tool for gaining deeper insights into steel corrosion mechanisms. EIS spectra unveil that steel corrosion is primarily controlled by the oxygen diffusion in a porous layer formed by iron oxides.

When aluminum and steel are in mechanical (and electrical) contact, the oxygen reduction reaction occurring on the porous layer atop the steel controls the corrosion of the galvanic pair in a 0.1 M Na_2SO_4 + 1 mM NaCl solution with a pH of 5.9. Despite the impedance of the system decreases as a function of time, it is likely attributed to the increased in surface area resulting from the porosity of the oxide layer on the steel, as measured by the evolution of L/r and Nr values.

As the surface area of the aluminum increases, the impedance also increases. This indicates that the corrosion process is slowed down. Additionally, it was shown that the cathodic reaction, which is most likely oxygen reduction, is kinetically controlled instead of diffusion-controlled.

6. References

(1) Stevens, K. J.; Lichti, K.; Minchington, I. A.; Janke-Gilman, N.; MacTutis, T.; Rook, D.; Bondurant, P. Conductor damage inspection system for overhead ACSR power cables CDIS on ACSR. In *Seventh International Conference on Sensing Technology*, Wellington, New Zealand 30 January 2014 2013; IEEE: pp 912-916. DOI: 10.1109/ICSensT.2013.6727780.

(2) Stevens, K. J.; Lichti, K.; Minchington, I. A.; Janke-Gilman, N.; Mactutis, T.; Rook, D.; Bondurant, P. Conductor damage inspection system for overhead ACSR power cables CDIS on ACSR. In *Seventh International Conference on Sensing Technology* 2013. DOI: 10.1109/ICSensT.2013.6727780.

(3) Havard, D. G.; Bellamy, G.; Buchan, P. G.; Ewing, H. A.; Horrocks, D. J.; Krishnasamy, S. G.; Motlis, J.; Yoshiki-Gravelsins, K. S. Aged ACSR conductors. I. Testing procedures for conductors and line items. *IEEE Transactions on Power Delivery* **1992**, *7* (2), 581-587. DOI: 10.1109/61.127052.

(4) Havard, D. G.; Bissada, M. K.; Fajardo, C. G.; Horrocks, D. J.; Meale, J. R.; Motlis, J. Y.; Tabatabai, M.; Yoshiki-Gravelsins, K. S. Aged ACSR conductors. II. Prediction of remaining life. *IEEE Transactions on Power Delivery* **1992**, *7* (2), 588-595. DOI: 10.1109/61.127053.

(5) Schwabe, P. H.; Pike, D. The measurement of corrosion in overhead power lines. *Anti-Corrosion Methods and Materials* **1988**, *35* (7), 4-5. DOI: 10.1108/eb020672.

(6) Rhaiem, E.; Bouraoui, T.; Halouani, F. E. Corrosion evolution of the aluminum alloys used in overhead transmission lines. *IOP Conference Series: Materials Science and Engineering* **2012**, *28*. DOI: 10.1088/1757-899x/28/1/012011.

(7) Isozaki, M.; Adachi, K.; Hita, T.; Asano, Y. Study of corrosion resistance improvement by metallic coating for overhead transmission line conductor. *Electrical Engineering in Japan* **2008**, *163* (1), 41-47. DOI: 10.1002/eej.20365.

(8) Ingle, A.; Heurtault, S.; Hafid, F.; Said, J.; Proietti, A.; Odemer, G.; Dehmas, M.; Blanc, C. Identification of the critical microstructural parameters on the corrosion behaviour of commercially pure aluminium alloy. *Corrosion Science* **2022**, *208*. DOI: 10.1016/j.corsci.2022.110654.

(9) Jones, D. A. *Principles and Prevention of Corrosion*; Pearson Education, 2013.

(10) Cross, S. R.; Gollapudi, S.; Schuh, C. A. Validated numerical modeling of galvanic corrosion of zinc and aluminum coatings. *Corrosion Science* **2014**, *88*, 226-233. DOI: 10.1016/j.corsci.2014.07.033.

(11) Magaino, S. i.; Soga, M.; Sobue, K.; Kawaguchi, A.; Ishida, N.; Imai, H. Zinc corrosion in simulated acid rain. *Electrochimica Acta* **1999**, *44* (24), 4307-4312. DOI: 10.1016/s0013-4686(99)00146-2.

(12) Thomas, S.; Birbilis, N.; Venkatraman, M. S.; Cole, I. S. Corrosion of Zinc as a Function of pH. *Corrosion* **2012**, *68* (1), 015009. DOI: 10.5006/1.3676630.

(13) Graedel, T. E. Corrosion Mechanisms for Zinc Exposed to the Atmosphere. *Journal of The Electrochemical Society* **1989**, *136* (4), 193C-203C. DOI: 10.1149/1.2096868.

(14) Ogle, K.; Morel, S.; Jacquet, D. Observation of Self-Healing Functions on the Cut Edge of Galvanized Steel Using SVET and pH Microscopy. *Journal of The Electrochemical Society* **2005**, *153* (1). DOI: 10.1149/1.2126577.

(15) Mansfeld, F.; Kenkel, J. V. Galvanic corrosion of Al alloys—III. The effect of area ratio. *Corrosion Science* **1975**, *15* (4), 239-250. DOI: 10.1016/s0010-938x(75)80019-9.

(16) Pryor, M. J.; Keir, D. S. Galvanic Corrosion: I . Current Flow and Polarization Characteristics of the Aluminum-Steel and Zinc-Steel Couples in Sodium Chloride Solution. *Journal of The Electrochemical Society* **1957**, *104* (5). DOI: 10.1149/1.2428559.

(17) Pryor, M. J.; Keir, D. S. Galvanic Corrosion: II . Effect of pH and Dissolved Oxygen Concentration on the Aluminum-Steel Couple. *Journal of The Electrochemical Society* **1958**, *105* (11). DOI: 10.1149/1.2428681.

(18) Lenderink, H. J. W.; Linden, M. V. D.; De Wit, J. H. W. Corrosion of aluminium in acidic and neutral solutions. *Electrochimica Acta* **1993**, *38* (14), 1989-1992. DOI: 10.1016/0013-4686(93)80329-x.

(19) Vujičić, V.; Lovreček, B. A Study of the influence of pH on the corrosion rate of aluminium. *Surface Technology* **1985**, *25* (1), 49-57. DOI: 10.1016/0376-4583(85)90047-0.

(20) Armstrong, R. D.; Braham, V. J. The mechanism of aluminium corrosion in alkaline solutions. *Corrosion Science* **1996**, *38* (9), 1463-1471. DOI: 10.1016/0010-938x(96)00037-6.

(21) Keddam, M.; Mattos, O. R.; Takenouti, H. Mechanism of anodic dissolution of iron-chromium alloys investigated by electrode impedances—I. Experimental results and reaction model. *Electrochimica Acta* **1986**, *31* (9), 1147-1158. DOI: 10.1016/0013-4686(86)80127-x.

(22) Benzekri, N.; Carranza, R.; Keddam, M.; Takenouti, H. AC response of RRDE during the passivation of iron. *Corrosion Science* **1990**, *31*, 627-635. DOI: 10.1016/0010-938x(90)90172-2.

(23) Colomban, P.; Cherifi, S.; Despert, G. Raman identification of corrosion products on automotive galvanized steel sheets. *Journal of Raman Spectroscopy* **2008**, *39* (7), 881-886. DOI: 10.1002/jrs.1927.

(24) Li, S.; Hihara, L. H. In situ Raman Spectroscopic Study of NaCl Particle-Induced Marine Atmospheric Corrosion of Carbon Steel. *Journal of The Electrochemical Society* **2012**, *159* (4), C147-C154. DOI: 10.1149/2.013204jes.

(25) Li, S.; Hihara, L. H. Aerosol Salt Particle Deposition on Metals Exposed to Marine Environments: A Study Related to Marine Atmospheric Corrosion. *Journal of The Electrochemical Society* **2014**, *161* (5), C268-C275. DOI: 10.1149/2.071405jes.

(26) Thébault, F.; Vuillemin, B.; Oltra, R.; Allely, C.; Ogle, K. Reliability of numerical models for simulating galvanic corrosion processes. *Electrochimica Acta* **2012**, *82*, 349-355. DOI: 10.1016/j.electacta.2012.04.068.

(27) Tada, E.; Sugawara, K.; Kaneko, H. Distribution of pH during galvanic corrosion of a Zn/steel couple. *Electrochimica Acta* **2004**, *49* (7), 1019-1026. DOI: 10.1016/j.electacta.2003.10.012.

(28) Calabrese, L.; Proverbio, E.; Pollicino, E.; Galtieri, G.; Borsellino, C. Effect of galvanic corrosion on durability of aluminium/steel self-piercing rivet joints. *Corrosion Engineering, Science and Technology* **2014**, *50* (1), 10-17. DOI: 10.1179/1743278214y.0000000168.

(29) Mouanga, M.; Puiggali, M.; Tribollet, B.; Vivier, V.; Pébère, N.; Devos, O. Galvanic corrosion between zinc and carbon steel investigated by local electrochemical impedance spectroscopy. *Electrochimica Acta* **2013**, *88*, 6-14, Article. DOI: 10.1016/j.electacta.2012.10.002 Scopus.

(30) Song, G.-L. Potential and current distributions of one-dimensional galvanic corrosion systems. *Corrosion Science* **2010**, *52* (2), 455-480. DOI: 10.1016/j.corsci.2009.10.003.

(31) Deshpande, K. B. Numerical modeling of micro-galvanic corrosion. *Electrochimica Acta* **2011**, *56* (4), 1737-1745. DOI: 10.1016/j.electacta.2010.09.044.

(32) Zhang, X. G.; Valeriote, E. M. Galvanic protection of steel and galvanic corrosion of zinc under thin layer electrolytes. *Corrosion Science* **1993**, *34* (12), 1957-1972. DOI: 10.1016/0010-938x(93)90053-j.

(33) Burczyk, L.; Darowicki, K. Local electrochemical impedance spectroscopy in dynamic mode of galvanic coupling. *Electrochimica Acta* **2018**, *282*, 304-310. DOI: 10.1016/j.electacta.2018.05.192.

(34) Tada, E.; Satoh, S.; Kaneko, H. The spatial distribution of Zn2+ during galvanic corrosion of a Zn/steel couple. *Electrochimica Acta* **2004**, *49* (14), 2279-2285. DOI: 10.1016/j.electacta.2004.01.008.

(35) Yin, L.; Jin, Y.; Leygraf, C.; Pan, J. A FEM model for investigation of micro-galvanic corrosion of Al alloys and effects of deposition of corrosion products. *Electrochimica Acta* **2016**, *192*, 310-318. DOI: 10.1016/j.electacta.2016.01.179.

(36) Yin, L.; Jin, Y.; Leygraf, C.; Pan, J. Numerical Simulation of Micro-Galvanic Corrosion of Al Alloys: Effect of Chemical Factors. *Journal of The Electrochemical Society* **2017**, *164* (13), C768-C778. DOI: 10.1149/2.0691713jes.

(37) Sung-Duck, K.; Morcos, M. M. Mechanical deterioration of ACSR conductors due to forest fires. *IEEE Transactions on Power Delivery* **2003**, *18* (1), 271-276. DOI: 10.1109/tpwrd.2002.804011.

(38) Barbosa, C. F.; Nallin, F. E. Corrosion detection robot for energized power lines. In Proceedings of the 2014 3rd International Conference on Applied Robotics for the Power Industry, 2014.

(39) Forrest, J. S.; Ward, J. M. Service experience of the effect of corrosion on steel-cored-aluminium overhead-line conductors. *Proceedings of the IEE - Part II: Power Engineering* **1954**, *101* (81), 271-283. DOI: 10.1049/pi-2.1954.0064.

(40) Zhang, X. G. Galvanic Corrosion of Zinc and Its Alloys. *Journal of The Electrochemical Society* **1996**, *143* (4), 1472-1484. DOI: 10.1149/1.1836662.

(41) Zhang, B.; Li, Y.; Wang, F. Electrochemical corrosion behaviour of microcrystalline aluminium in acidic solutions. *Corrosion Science* **2007**, *49* (5), 2071-2082. DOI: 10.1016/j.corsci.2006.11.006.

(42) Mansfeld, F. Area Relationships in Galvanic Corrosion. *Corrosion* **1971**, *27* (10), 436-442. DOI: 10.5006/0010-9312-27.10.436.

(43) Tavakkolizadeh, M.; Saadatmanesh, H. Galvanic Corrosion of Carbon and Steel in Aggressive Environments. *Journal of Composites for Construction* **2001**, *5* (3), 200-210. DOI: 10.1061/(asce)1090-0268(2001)5:3(200).

(44) Tran, A. T.; Huet, F.; Ngo, K.; Rousseau, P. Artefacts in electrochemical impedance measurement in electrolytic solutions due to the reference electrode. *Electrochimica Acta* **2011**. DOI: 10.1016/j.electacta.2010.12.088.

(45) Guseva, O.; Schmutz, P.; Suter, T.; von Trzebiatowski, O. Modelling of anodic dissolution of pure aluminium in sodium chloride. *Electrochimica Acta* **2009**, *54* (19), 4514-4524. DOI: 10.1016/j.electacta.2009.03.048.

(46) Na, K.-H.; Pyun, S.-I. Effect of sulphate and molybdate ions on pitting corrosion of aluminium by using electrochemical noise analysis. *Journal of Electroanalytical Chemistry* **2006**, *596* (1), 7-12. DOI: 10.1016/j.jelechem.2006.06.017.

(47) Mrema, E.; Itoh, Y.; Kaneko, A.; Hirohata, M. Galvanic corrosion study of aluminium alloy plates mounted to stainless and mild steel bolts by accelerated exposure test. *構造工学論文集 A* **2016**, *62A*, 525-536. DOI: 10.11532/structcivil.62A.525.

(48) Dafydd, H.; Worsley, D. A.; McMurray, H. N. The kinetics and mechanism of cathodic oxygen reduction on zinc and zinc–aluminium alloy galvanized coatings. *Corrosion Science* **2005**, *47* (12), 3006-3018. DOI: 10.1016/j.corsci.2005.05.036.

(49) Benoit, M.; Bataillon, C.; Gwinner, B.; Miserque, F.; Orazem, M. E.; Sánchez-Sánchez, C. M.; Tribollet, B.; Vivier, V. Comparison of different methods for measuring the passive film thickness on metals. *Electrochimica Acta* **2016**, *201*, 340-347. DOI: 10.1016/j.electacta.2015.12.173.

(50) Chen, Y.-M.; Rudawski, N. G.; Lambers, E.; Orazem, M. E. Application of Impedance Spectroscopy and Surface Analysis to Obtain Oxide Film Thickness. *Journal of The Electrochemical Society* **2017**, *164* (9), C563-C573. DOI: 10.1149/2.1061709jes.

(51) Gharbi, O.; Tran, M. T. T.; Orazem, M. E.; Tribollet, B.; Turmine, M.; Vivier, V. Impedance Response of a Thin Film on an Electrode: Deciphering the Influence of the Double Layer Capacitance. *ChemPhysChem* **2021**, *22* (13), 1371-1378, Article. DOI: 10.1002/cphc.202100177 Scopus.

(52) Hirschorn, B.; Orazem, M. E.; Tribollet, B.; Vivier, V.; Frateur, I.; Musiani, M. Constant-Phase-Element Behavior Caused by Resistivity Distributions in Films. *Journal of The Electrochemical Society* **2010**, *157* (12). DOI: 10.1149/1.3499565.

(53) Huang, V. M.-W.; Vivier, V.; Orazem, M. E.; Pébère, N.; Tribollet, B. The Apparent Constant-Phase-Element Behavior of an Ideally Polarized Blocking Electrode. *Journal of The Electrochemical Society* **2006**, *154* (2). DOI: 10.1149/1.2398882.

(54) Orazem, M. E.; Pébère, N.; Tribollet, B. Enhanced Graphical Representation of Electrochemical Impedance Data. *Journal of The Electrochemical Society* **2006**, *153* (4). DOI: 10.1149/1.2168377.

(55) You, C.; Dizon, A.; Gao, M.; Vivier, V.; Orazem, M. E. Experimental observation of ohmic impedance. *Electrochimica Acta* **2022**, *413*. DOI: 10.1016/j.electacta.2022.140177.

(56) Barcia, O. E.; Cattarin, S.; D'Elia, E.; Frateur, I.; Mattos, O. R.; Musiani, M.; Pébère, N.; Tribollet, B. Further to the paper "Application of the impedance model of de Levie for the characterization of porous electrodes" by Barcia et al. [Electrochim. Acta 47 (2002) 2109]. *Electrochimica Acta* **2006**, *51* (10), 2096-2097. DOI: 10.1016/j.electacta.2005.06.035.

(57) Barcia, O. E.; D'Elia, E.; Frateur, I.; Mattos, O. R.; Pébère, N.; Tribollet, B. Application of the impedance model of de Levie for the characterization of porous electrodes. *Electrochimica Acta* **2002**, *47* (13-14), 2109-2116. DOI: 10.1016/s0013-4686(02)00081-6.

(58) Frateur, I.; Deslouis, C.; Orazem, M. E.; Tribollet, B. Modeling of the cast iron/drinking water system by electrochemical impedance spectroscopy. *Electrochimica Acta* **1999**, *44* (24), 4345-4356. DOI: 10.1016/s0013-4686(99)00150-4.

(59) Lasia, A. *Electrochemical Impedance Spectroscopy and its Applications*; Springer New York, NY, 2014. DOI: 10.1007/978-1-4614-8933-7.

(60) *EIS: Measurement Model Program*; OSF: 2020. (accessed.

(61) Simillion, H.; Van den Steen, N.; Terryn, H.; Deconinck, J. Geometry influence on corrosion in dynamic thin film electrolytes. *Electrochimica Acta* **2016**, *209*, 149-158. DOI: 10.1016/j.electacta.2016.04.072.

(62) Tran, V. N.; Ooi, A.; Tada, E.; Nishikata, A. EIS Characteristics of Galvanic Couple of Aluminum Alloy and High-strength Steel under Thin Solution Films. *Journal of The Electrochemical Society* **2020**, *167* (13). DOI: 10.1149/1945-7111/abbb44.

(63) Foroulis, Z. A.; Thubrikar, M. J. On the Kinetics of the Breakdown of Passivity of Preanodized Aluminum by Chloride Ions. *Journal of The Electrochemical Society* **1975**, *122* (10), 1296-1301. DOI: 10.1149/1.2134003.

(64) Onn, T. M.; Monai, M.; Dai, S.; Arroyo-Ramirez, L.; Zhang, S.; Pan, X.; Graham, G. W.; Fornasiero, P.; Gorte, R. J. High-surface-area, iron-oxide films prepared by atomic layer deposition on γ-Al2O3. *Applied Catalysis A: General* **2017**, *534*, 70-77. DOI: 10.1016/j.apcata.2017.01.025.

(65) Stratmann, M. The Atmospheric Corrosion of Iron — A Discussion of the Physico-Chemical Fundamentals of this Omnipresent Corrosion Process Invited Review. *Berichte der Bunsengesellschaft für physikalische Chemie* **1990**, *94* (6), 626-639. DOI: 10.1002/bbpc.19900940603.

(66) Pedersen, C.; Aslyamov, T.; Janssen, M. Equivalent Circuit and Continuum Modeling of the Impedance of Electrolyte-Filled Pores. *PRX Energy* **2023**, *2* (4). DOI: 10.1103/PRXEnergy.2.043006.

(67) Jurczakowski, R.; Hitz, C.; Lasia, A. Impedance of porous Au based electrodes. *Journal of Electroanalytical Chemistry* **2004**, *572* (2), 355-366. DOI: 10.1016/j.jelechem.2004.01.008.

(68) DiBari, G. A.; Read, H. J. Electrochemical Behavior of High Purity Aluminum in Chloride Containing Solutions. *Corrosion* **1971**, *27* (11), 483-494. DOI: 10.5006/0010-9312-27.11.483.

(69) Kolics, A.; Polkinghorne, J. C.; Wieckowski, A. Adsorption of sulfate and chloride ions on aluminum. *Electrochimica Acta* **1998**, *43* (18), 2605-2618. DOI: 10.1016/s0013-4686(97)10188-8.

(70) Moshier, W. C.; Davis, G. D.; Ahearn, J. S. The corrosion and passivity of aluminum exposed to dilute sodium sulfate solutions. *Corrosion Science* **1987**, *27* (8), 785-801. DOI: 10.1016/0010-938x(87)90037-0.

(71) Tan, T. C.; Chin, D. T. Polarization of Aluminum during AC Corrosion in Sulfate Solutions. *Journal of The Electrochemical Society* **1985**, *132* (4), 766-773. DOI: 10.1149/1.2113955.

(72) Macdonald, D. D. On the Formation of Voids in Anodic Oxide Films on Aluminum. *Journal of The Electrochemical Society* **1993**, *140* (3), L27-L30. DOI: 10.1149/1.2056179.

(73) Lyon, S. B.; Thompson, G. E.; Johnson, J. E.; Wood, G. C.; Ferguson, J. M. Accelerated Atmospheric Corrosion Testing Using a Cyclic Wet/Dry Exposure Test:Galvanic Couples of Aluminum with Graphite Neoprene Rubber, Galvanized Steel, and Steel. *Corrosion* **1989**, *45* (11), 951-957. DOI: 10.5006/1.3585006.

(74) Håkansson, E.; Hoffman, J.; Predecki, P.; Kumosa, M. The role of corrosion product deposition in galvanic corrosion of aluminum/carbon systems. *Corrosion Science* **2017**, *114*, 10-16. DOI: 10.1016/j.corsci.2016.10.011.

(75) Hakansson, E.; Predecki, P.; Kumosa, M. S. Galvanic Corrosion of High Temperature Low Sag Aluminum Conductor Composite Core and Conventional Aluminum Conductor Steel Reinforced Overhead High Voltage Conductors. *IEEE Transactions on Reliability* **2015**, *64* (3), 928-934. DOI: 10.1109/tr.2015.2427894.

(76) Xavier, J. R.; Nishimura, T. Galvanic corrosion behaviour of iron coupled to aluminium in NaCl solution by scanning eectrochemical microscopy. *Protection of Metals and Physical Chemistry of Surfaces* **2016**, *52* (3), 543-554. DOI: 10.1134/s2070205116030242.

(77) Kosaba, T.; Muto, I.; Sugawara, Y. Galvanic Corrosion Processes of Aluminum Coupled to Iron in Chloride Solutions at Near-Neutral pH. *ECS Meeting Abstracts* **2019**, *MA2019-02* (54), 2404. DOI: 10.1149/MA2019-02/54/2404.

(78) Liu, J.; Huang, X.; Ren, Y.; Wong, L. M.; Liu, H.; Wang, S. Galvanic corrosion protection of Al-alloy in contact with carbon fibre reinforced polymer through plasma electrolytic oxidation treatment. *Sci Rep* **2022**, *12* (1), 4532. DOI: 10.1038/s41598-022-08727-7 From NLM PubMed-not-MEDLINE.

(79) Policastro, S. A.; Anderson, R. M.; Hangarter, C. M. Analysis of Galvanic Corrosion Current between an Aluminum Alloy and Stainless-Steel Exposed to an Equilibrated Droplet

Electrolyte. *Journal of The Electrochemical Society* **2021**, *168* (4). DOI: 10.1149/1945-7111/abf5a7.

(80) Zhu, H.; Huang, Z.; Jin, G.; Gao, M. Effect of temperature on galvanic corrosion of Al 6061-SS 304 in nitric acid. *Energy Reports* **2022**, *8*, 112-123. DOI: 10.1016/j.egyr.2022.10.022.

(81) Lampeas, N.; Koutsoukos, P. G. The importance of the solution pH in electrochemical studies of aluminum in aqueous media containing chloride. *Corrosion Science* **1993**, *36* (6), 1011-1025. DOI: 10.1016/0010-938x(94)90200-3.

(82) McCafferty, E. Sequence of steps in the pitting of aluminum by chloride ions. *Corrosion Science* **2003**, *45* (7), 1421-1438. DOI: 10.1016/s0010-938x(02)00231-7.

(83) Natishan, P. M.; O'Grady, W. E. Chloride Ion Interactions with Oxide-Covered Aluminum Leading to Pitting Corrosion: A Review. *Journal of The Electrochemical Society* **2014**, *161* (9), C421-C432. DOI: 10.1149/2.1011409jes.